MRC/ABQ-R-1909
Copy 1

Mission Research Corporation

Beam-Target Interactions in Single- and Multi-Pulse Radiography

Final Report

Bryan V. Oliver
Dale R. Welch
Thomas P. Hughes

April 1999

Prepared for: LAWRENCE LIVERMORE NATIONAL LABORATORY
P.O. Box 808
7000 East Avenue
Livermore, CA 94550

Under Contract: LLNL B347781

Prepared by: MISSION RESEARCH CORPORATION
1720 Randolph Road, SE
Albuquerque, NM 87106-4245
(505) 768-7600

DISCLAIMER

Contents

List of Figures

1 Introduction

This report describes calculations concerning the interaction of intense electron beam pulses with a solid target. In Section 2, we treat the propagation of a beam pulse through a dense plasma plume in front of the target, resulting from material blown off from the target by prior pulses. Because of the short magnetic decay-time, the primary effect of the plasma is to shift the focal spot of the beam longitudinally by an amount which is constant over most of the beam pulse. It may be possible to compensate for this effect by changing the upstream focusing elements from one beam pulse to the next. Section 3 describes a mechanism by which lighter ion species can diffuse to the surface of a plasma plume, thereby potentially increasing the concentration of bulk contaminant species such as hydrogen at the leading edge of the plume. These ions could then become a light-ion source for subsequent beam pulses. Based on the calculations, we tentatively recommend bulk contaminant fractions be limited to 10^{-5}–10^{-4}. In Section 4, we estimate the number of adsorbed monolayers needed to provide a space-charge-limited (SCL) ion source at the target for the initial beam pulse. We find that ≈ 10 monolayers are required for SCL emission of H_2^+ ions. This may explain why there was little evidence of focus disruption in ETA-II target experiments.

2 Intense E-Beam Propagation in Over-Dense Plasma

B. Oliver

2.1 Introduction

A detailed study of the beam dynamics in the presence of an over-dense plasma column is given. The proposed use of intense electron beams as a source for x-ray driven Advanced Hydrodynamic Radiography requires beam spot sizes using Linear Induction Accelerator (LIA) technology of less than a millimeter and currents of 3 kA at energies of 40 MeV. The e-beam is focused onto a high atomic number (Z) target producing bremsstrahlung x-ray radiation. Typical pulse-lengths τ of order 50 ns with up to six pulses separated by $\sim$ 350 ns (for a total duration of $\sim$ 2 μs) are anticipated for an Advanced Hydro Facility (AHF). At these intensities and pulse durations the e-beam can readily melt the target material and cause a plasma plume to propagate outward into the path of subsequent pulses. The interaction of the beam with the cool, expanding plasma can result in increased beam spot and emittance on target.

For a LIA driven beam, normal transport to the target occurs in vacuum. The beam is neither charge nor current neutralized and confinement and final focusing is achieved with magnetic lenses. If the beam encounters an over-dense plasma such that the plasma density satisfies $Zn_p \gg n_b$, where n_b is the e-beam density and Z is the plasma charge state, then the plasma will effectively neutralize the beam space-charge and current on a timescale of order the inverse electron plasma frequency $1/\omega_{pe} = (4\pi Z^2 e^2 n_p/m_e)^{-1/2} \ll \tau$. For emittance dominated beams (as is the case after final focus to the target) this poses little effect to the beam propagation characteristics, since for such beams the propagation is nearly ballistic (i.e., no net forces act on the beam).

On the other hand, near the target the e-beam radius is typically sub-millimeter, thus for even high conductivity plasmas with conductivities $\sigma \geq 10^{14}$ s, the magnetic diffusion time $t_d = (2\pi\sigma r_b^2)/c^2$ is of the order $t_d \sim 10$ ns for $r_b \sim 1$ mm. Indeed, at the focal/target plane, $r_b \sim 0.4$ mm such that t_d is even shorter and the diffusion time satisfies $t_d \ll \tau$. For times intermediate to t_d and τ the beam will be fully current un-neutralized but will remain charge neutralized (plasma ions will remain confined by the e-beam space-charge potential). As such,

the beam will propagate in a self-pinched mode. In this configuration the beams' self-field acts as an additional focusing lens which can lead to adverse focal properties at the target.

A review of the characteristics and analytic theory of beam propagation in plasma is given in Section 2.2. This is followed in Section 2.3 by results from simulation of an AHF parameter beam propagating to the target in 1-3 cm length plasma columns. Simulations are conducted with the hybrid PIC/fluid code TEPID (target electron plasma interaction dynamics). Discussion of the simulation results and mitigation methods are presented in Section 2.4.

2.2 Beam/Plasma dynamics

An illustration of the beam propagation geometry is given in Figure 1. We are concerned with the propagation characteristics of the beam within the plasma plume. Hydrodynamic calculations with the LASNEX code indicate that a typical environment near the target will consist of a plume approximately 3 cm in length with density $Zn_p \sim 10^{16}$ cm^{-3} and electron temperature $T_e \leq 6$ eV [1]. Prior to entering the plume the beam dynamics are well described by the paraxial envelope equation for propagation in vacuum. We therefore only consider changes to the dynamics in the region occupied by the plasma. For a uniform beam with emittance $\epsilon = 0.15$ rad-cm, impinging the target with a 1 mm focal spot, the beam parameters 3 cm from the target are $r_b = 0.11$ cm with a macro-angle $\Theta = 28$ mrad. Model equations describing the anticipated plasma dynamics as well as the corresponding beam dynamics are given below.

2.2.1 Plasma model

The plasma is modeled in the electron magnetohydrodynamic limit (EMHD) where plasma ion motion is neglected and all current is carried by the electrons. Plasma electrons are included as a cold, inertialess, resistive, fluid. The plasma current is therefore described by the generalized Ohm's law (derived from the electron equation of motion with $m \to 0$):

$$\mathbf{E} = \frac{1}{en_e c}(\mathbf{j_e} \times \mathbf{B}) + \frac{1}{\sigma}\mathbf{j_e}, \tag{1}$$

where $\mathbf{j_e} = -en_e\mathbf{v_e}$ is the electron current density, n_e the plasma electron density, and σ the plasma conductivity. All other symbols have their usual meaning and Gaussian units are used throughout. Although the plasma ions are considered immobile on the timescales of interest,

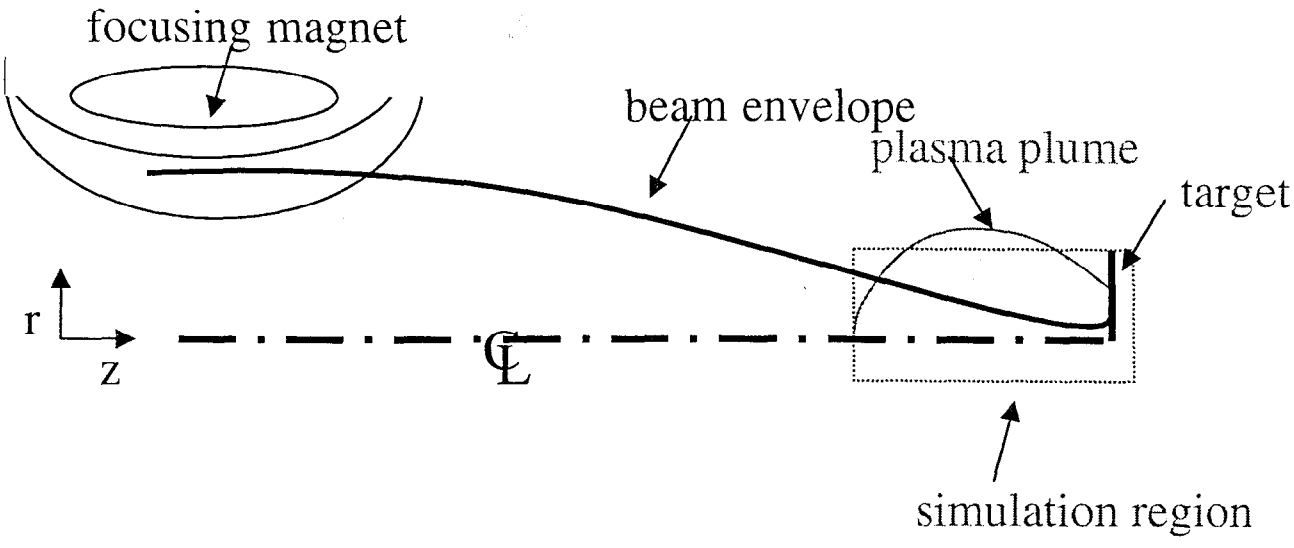

Figure 1: The beam propagation geometry.

qausi-neutrality is assumed such that $n_e = Zn_p - n_b$. The assumption of quasi-neutrality is reasonable for plasma densities satisfying $Zn_p/n_b \geq 5$.

The EMHD plasma limit is generally valid for timescales short compared to the ion gyro-frequency $\Omega_i = ZeB/Mc$ and lengthscales short compared to the ion inertial length c/ω_{pi} [2]. For the problems of interest here, the maximum magnetic field $B_\theta = 2I_b/cr_b \simeq 5$ kG for a beam current $I_b = 3$ kA and radius $r_b = 1$ mm. Hence, for pulse-lengths $\tau = 50$ ns, the ratio $(\Omega_i\tau/2\pi) \sim 10^{-1}$–$10^{-2}$ for plasma ions H^+–Ta^{+6}. And for typical length-scales of order the beam radius $(r_b\omega_{pi}/c) \sim 10^{-2}$ for plasma densities $Zn_p \sim 10^{16}$ cm^{-3}.

The electron current is related to the magnetic field and the beam current $\mathbf{j_b} = -en_b\mathbf{v_b}$ via Ampere's law with the displacement current neglected:

$$\mathbf{j_e} = \frac{c}{4\pi}\nabla \times \mathbf{B} - \mathbf{j_b}. \tag{2}$$

An induction equation for the magnetic field is obtained from the curl of Eq. (1). Substitution of Eq. (2) into the resulting induction equation yields an evolution equation for $\mathbf{B}$ which is strictly a function of the beam current density and the plasma parameters σ and n_e

$$\frac{\partial \mathbf{B}}{\partial t} + \nabla \times \frac{c}{4\pi e n_e}\left(\nabla \times \mathbf{B} - \frac{4\pi}{c}\mathbf{j_b}\right) \times \mathbf{B} = \nabla \times \frac{c^2}{4\pi\sigma}\left(\nabla \times \mathbf{B} - \frac{4\pi}{c}\mathbf{j_b}\right). \tag{3}$$

For a known beam particle and current density, Eq. (3) represents a self-consistent calculation of the magnetic field (and hence the net current) in the plasma. The second term on the lhs of Eq. (3) describes advection of the magnetic field with the plasma electron fluid and is a consequence of the Hall term in Eq. (1). The term on the rhs describes diffusion of the return current. The beam particle evolutions are solved consistently via the Lorentz force equation

$$m\frac{d\gamma \mathbf{v_b}}{dt} = -e\left(\mathbf{E} + \frac{1}{c}\mathbf{v_b} \times \mathbf{B}\right) \tag{4}$$

by the Particle in Cell (PIC) method outlined in Section 2.3. The beam density and current density are obtained from the appropriate moments of the particle distribution.

For axisymmetric plasmas and beam distributions (i.e., $\partial_\theta = 0$), and for beam particles with zero angular momentum, the only component of $\mathbf{B} = B_\theta \hat{\theta}$.

2.2.2 Beam envelope dynamics

Although we numerically solve the beam evolution consistently with the plasma dynamics via Eq. (4), a simple picture of the evolution from consideration of the beam envelope equation is pertinent. For relativistic electron beams, the envelope radius r_b is described by the paraxial ray equation [3]

$$\frac{d^2 r_b}{dz^2} = \frac{2\nu}{\beta^2\gamma}[1 - f_e - (1 - f_b)\beta^2]\frac{1}{r_b} + \frac{\epsilon^2}{\gamma^2\beta^2}\frac{1}{r_b^3}, \tag{5}$$

where the independent variable z is the propagation axis, ϵ (rad-cm) is the beam emittance, ν is Budker's parameter which is related to the normalized beam current $\nu \equiv [I_b/17(\mathrm{kA})\beta]$, β is the normalized beam velocity $\beta = v_b/c$, and γ is the relativistic factor. In Eq. (5) the coefficients f_e and f_b are the fraction of beam charge and current neutralization, respectively. In vacuum, $f_e = f_b = 0$. For propagation in a resistive, over-dense plasma, and for times $t > 1/\omega_{pe}$, the charge neutralization fraction $f_e = 1$ and the current neutralization fraction $1 > f_b(t) \geq 0$. In particular, for times $t \gg t_d$, the beam current is fully unneutralized, $f_b \to 0$, and Eq. (5) becomes

$$\frac{d^2 r_b}{dz^2} = \frac{-2\nu}{\gamma}\frac{1}{r_b} + \frac{\epsilon^2}{\gamma^2\beta^2}\frac{1}{r_b^3}. \tag{6}$$

If the beam emittance is conserved, it proves useful to normalize r_b to the equilibrium (matched) beam radius $a = (\epsilon/\sqrt{2\nu\gamma\beta^2})$ and z to the betatron wavelength $\lambda = (\epsilon/2\nu\beta)$. In the normalized variables, Eq. (6) becomes

$$\frac{d^2 r}{dz^2} = -\frac{1}{r} + \frac{1}{r^3}, \tag{7}$$

where the subscript b has been dropped for convenience. From the first integral of Eq. (7), the dynamics of the beam envelope are completely determined by the Hamiltonian

$$H = \frac{1}{2}\left(\frac{dr}{dz}\right)^2 + \ln(r) + \frac{1}{2r^2}. \tag{8}$$

Equation (8) describes the periodic oscillations of a particle in a potential

$$\phi(r) = \ln(r) + \frac{1}{2r^2}.$$

The potential $\phi(r)$ is plotted in Figure 2 (a).

For perturbations about the equilibrium energy $H = 1/2$, corresponding to the matched beam condition $r_b = a$, the beam envelope oscillates harmonically with wavenumber $k_0 = \sqrt{2}/\lambda$. For larger energies, the envelope oscillations are strongly anharmonic with normalized inverse wavenumber (oscillation period)

$$\frac{1}{k} = \frac{1}{\pi}\int_{r_{\min}}^{r_{\max}} \frac{dr}{\sqrt{2H - 2\ln(r) - 1/r^2}}, \tag{9}$$

where $r_{\min}$ and $r_{\max}$ are the minimum and maximum envelope radii, respectively. The values $r_{\min}$ and $r_{\max}$ are given by the roots of the transcendental equation $\phi(r) = H$. For normal injection into the plasma region [i.e., $(dr/dz) = 0$] the value $F = \pi/k$ represents the distance to the first minimum of the beam envelope and is equivalent to the focal plane for a beam focused by a magnetic lens comprised entirely of its own self-field. A plot of F vs. H is given in Figure 2 (b). Note the limiting value of $F \to \pi/\sqrt{2}$ as $H \to 1/2$.

2.3 Simulation results

TEPID is a cylindrically symmetric hybrid code which has been adapted from the Solenz code [2] for the study of relativistic electron beams in plasma. The Eqs. (1) and (3) for the plasma response are solved via finite difference on a fixed Eulerian grid in the (r, z) plane. The electron beam particle orbits (positions and velocities) are calculated self-consistently from Eq. (4) in the PIC limit after obtaining the fields $\mathbf{E}$ and $\mathbf{B}$ from (1) and (3), respectively. The beam density n_b and current density $\mathbf{j_b}$ are solved from the appropriate moments of the beam particle distribution.

For the simulations reported here the beam parameters are between 2.7–3 kA current, 40 MeV energy, with emittance $\epsilon = 0.15$ rad-cm. The beam pulselength $\tau = 50$ ns. This

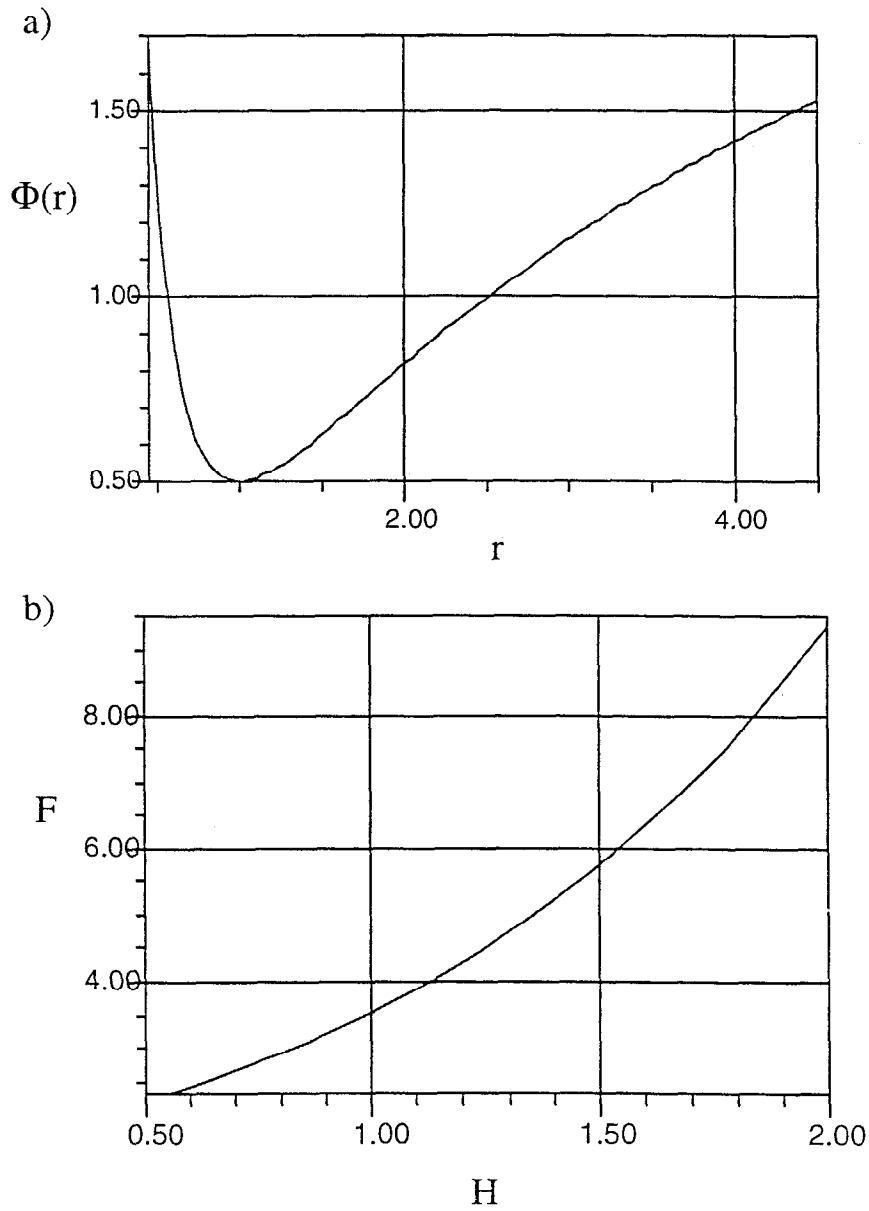

Figure 2: (a) The beam envelope potential $\phi(r)$ and (b) the distance of the first envelope minimum as a function of the beam injection energy H for normal ($dr/dz = 0$) injection.

corresponds to $\gamma \simeq 79$ and $\nu \simeq 0.17$, and a matched beam radius $a = 0.03$ cm and betatron wavelength $\lambda = 0.45$ cm. The initial injection root-mean squared radius (rms) $r_i = 0.08$ cm and initial macro-angle of injection $\Theta = 28$ mrad. For vacuum transport, these initial conditions yield an rms beam radius at focus $r_f = 0.045$ cm at a focal plane 3 cm downstream of the injection plane. For a uniform density profile, the beam envelope radius is $r_b = \sqrt{2} r_{rms}$. A plot of the beam configuration (r, z) space and phase space $(r, v_r/c)$ at the target is given in Figure 3 for the case of vacuum transport (i.e., no plasma field interaction) and a Gaussian beam profile. The injection plane is at $z = 0$ and the target is located at $z = 3$ cm. In Figure 4 the beams' root-mean-squared radius r_{rms} and emittance ϵ at a) the injection plane and b) the target are plotted. Note that in this case without plasma interaction the emittance is conserved during propagation.

The plasma parameters are held constant with $Zn_p = 10^{16}$ cm^{-3} and $\sigma = 1.3 \times 10^{14}$ s^{-1}. For a Spitzer conductivity $\sigma = (\omega_{pe}^2/4\pi\nu_{ei})$, where $\nu_{ei} = 2.9 \times 10^{-6} \Lambda Z n_p T_e^{-3/2}$ is the Coulomb collision frequency, the value of σ corresponds to a plasma with electron temperature $T_e \sim 6$ eV. Importantly, for Spitzer like values, the plasma conductivity is only weakly dependent on density through the Coulomb logarithm Λ and, therefore, spatially dependent densities have little effect on the diffusive properties of the plasma. For these parameters, the characteristic magnetic diffusion time $t_d = (2\pi\sigma r^2/c^2) \equiv (r^2\omega_{pe}^2/2c^2\nu_{ei})$ is approximately 6 ns at $r = r_i$ and 1.2 ns at $r = r_f$. Both times are much shorter than the beam time τ.

Results from propagation within the target plasma column are presented in Figures 5–7 for beams with a Gaussian and a uniform current density profile at injection. In Figures 5 and 6 the configuration and phase space are plotted at time $t = 40$ ns for the Gaussian and uniform distribution beams, respectively. Compared to the results plotted in Figure 3, it is clear that the beam has been pinched and pre-focuses, resulting in a large spot at the target. The r_{rms} radius and ϵ are plotted in Figure 7 as a function of time at the target plane ($z = 3$ cm) for both distributions. The radius at first decreases, pinching to less than 0.025 cm, but then rapidly increases as the focal point of the beam sweeps backwards away from the target plane. The beam is now over-focused and hence, obtains a small spot at a distance in front of the target and then spreads out to large radius at the target [this is evidenced in Figures 5 (a) and 6 (a)]. By the time $t = 10$ ns, both beams are near equilibrium, with a time independent $r_{rms} \simeq 0.065$ cm. Note that this time is in close agreement with the diffusion time $t_d \simeq 6$ ns at $r = r_i$, demonstrating that the plasma return current has nearly decayed to zero and the full

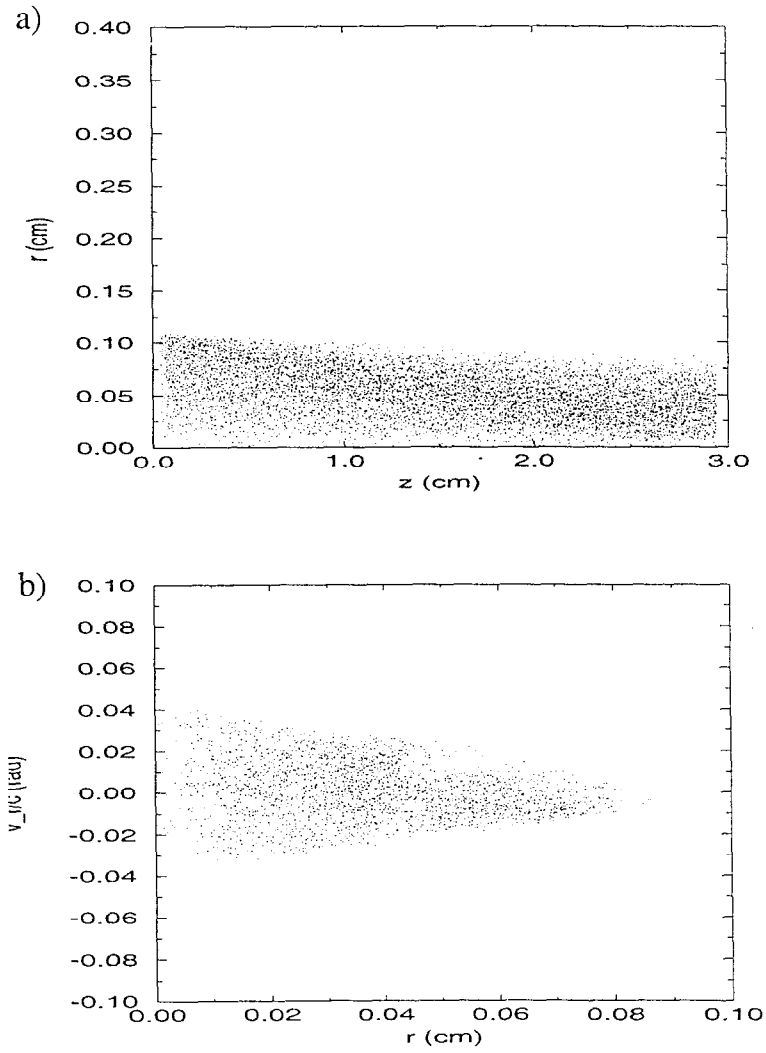

Figure 3: The beam (a) configuration space and (b) phase-space at the target position $z = 3$ cm, for the case of vacuum transport.

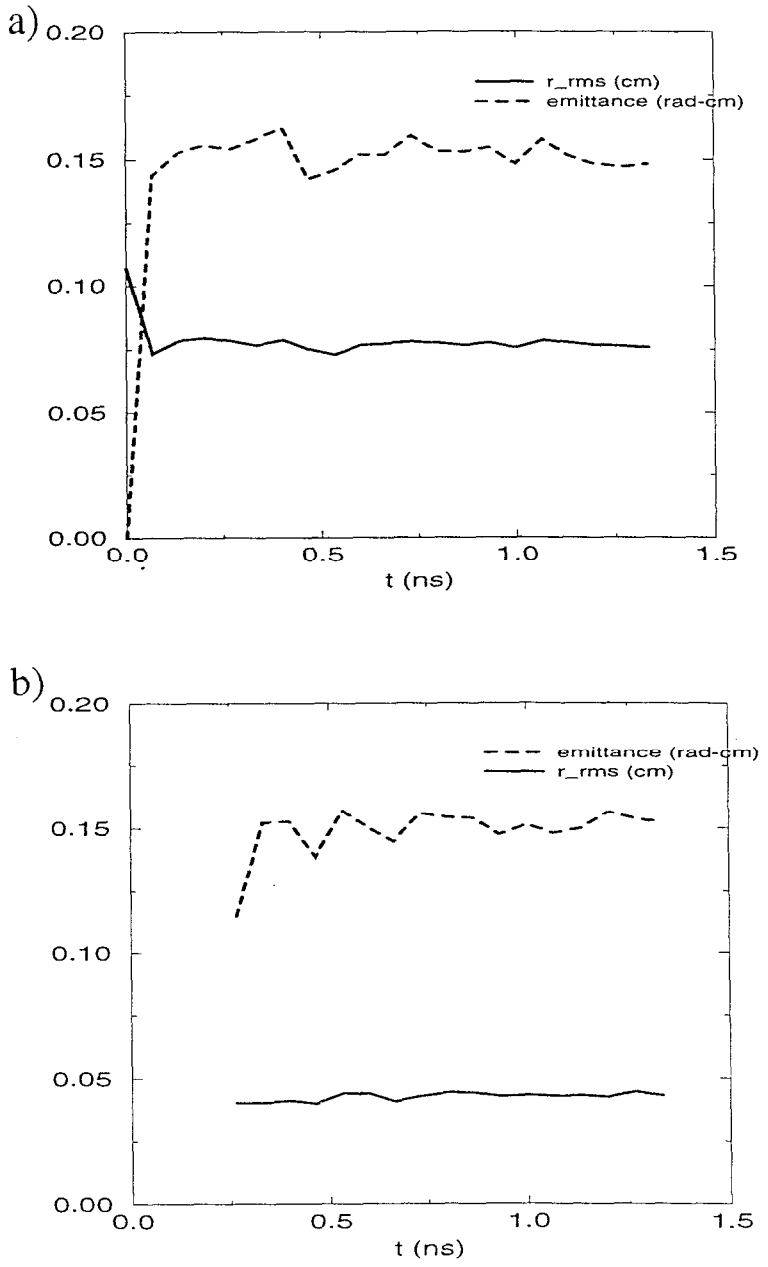

Figure 4: The beam emittance (dashed line) and r_{rms} (solid line) radius at (a) injection $z = 0$ and (b) at the target position $z = 3$ cm, for the case of vacuum transport.

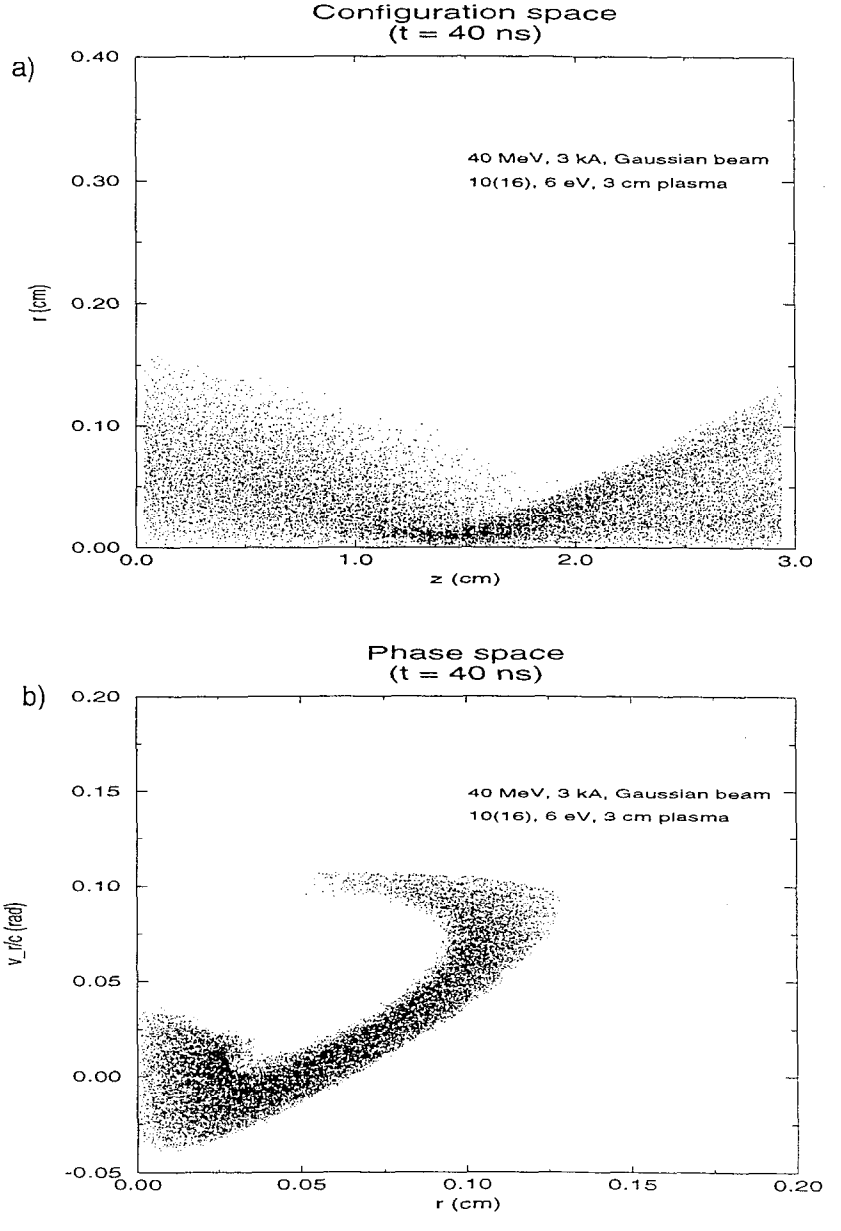

Figure 5: The beam (a) configuration space and (b) phase-space at the target position $z = 3$ cm, for the case of propagation in a 3 cm long plasma. The initial beam distribution is Gaussian. Beam parameters are 3 kA, 40 MeV, $\epsilon = 0.15$ rad-cm.

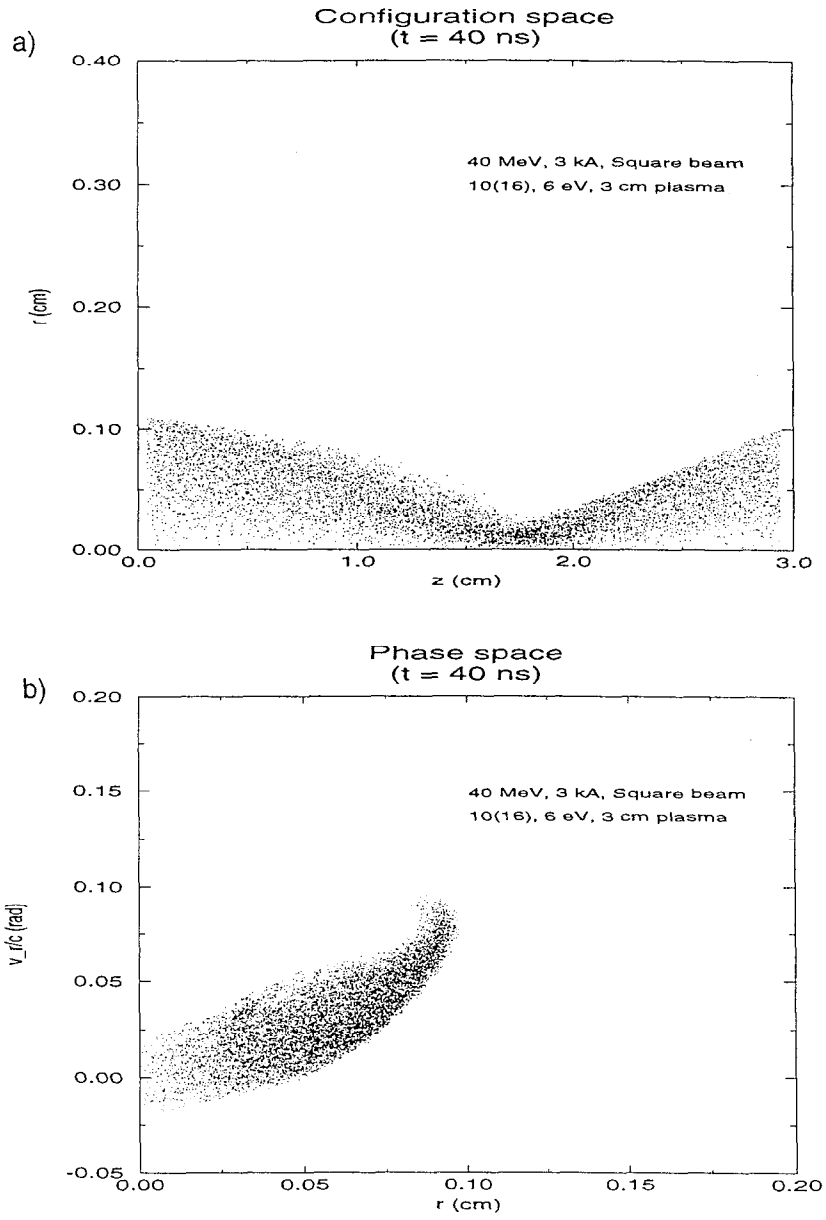

Figure 6: The beam (a) configuration space and (b) phase-space at the target position $z = 3$ cm, for the case of propagation in a 3 cm long plasma. The initial beam distribution is uniform. Beam parameters are 3 kA, 40 MeV, $\epsilon = 0.15$ rad-cm.

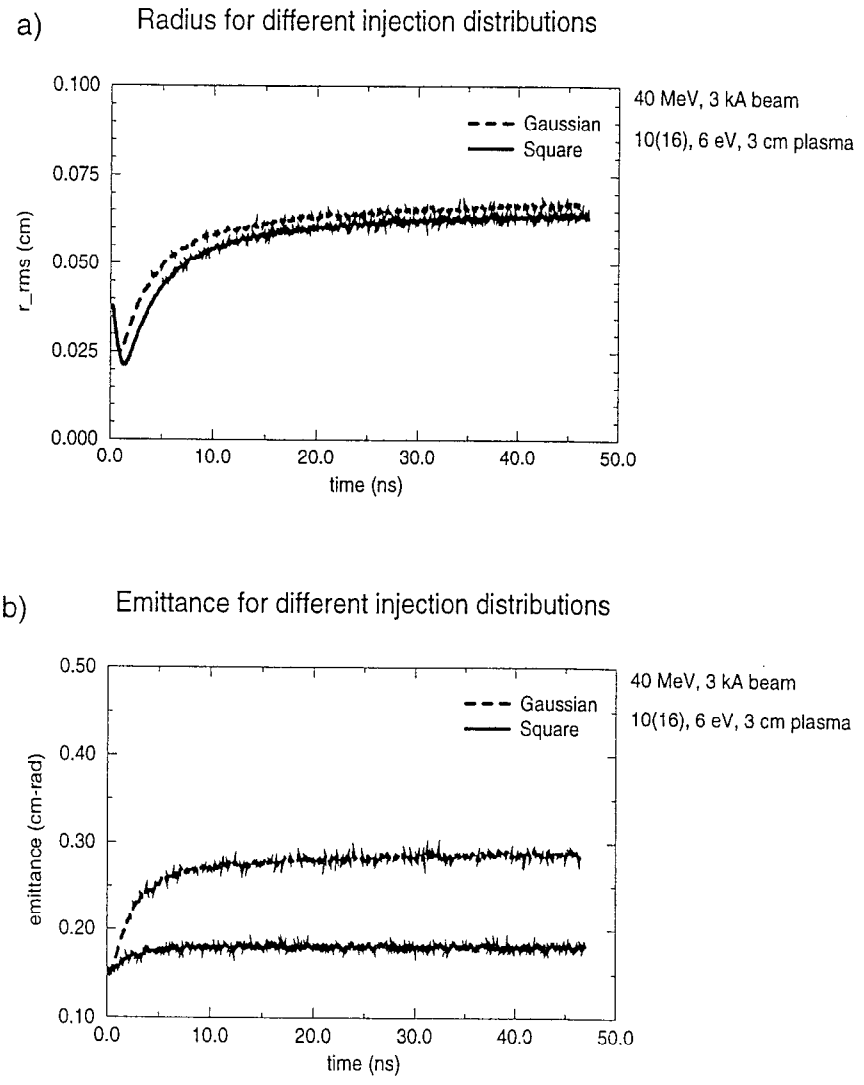

Figure 7: The beam (a) root-mean-squared radius (b) emittance at the target as functions of time. Results for both the initial Gaussian distribution (dashed) and uniform distribution (solid) are plotted.

beam current is exposed. Thus in Eq. (5) $f_b \to 0$, while $f_e = 1$ is maintained by the assumption of quasi-neutrality.

According to the discussion of Section 2.2.2, the new focal plane should be a function of the injection energy H and of order λ. For the uniform beam profile given in Figure 6 the beam envelope at injection $r_b = \sqrt{2} r_i = 0.11$ cm, which is equivalent to a normalized envelope radius $r = r_b/a = 3.7$. The normalized injection macro angle $(dr/dz) = \Theta(\lambda/a) = 0.42$. Hence, from Eq. (8) the Hamiltonian $H \simeq 1.4$. This results in a calculated minimum radius $r_{\min} = 0.5$, or equivalently in unnormalized units $r_b|_{\min} = 0.5a = 0.015$ cm. The distance to first focal plane is given by Eq. (9) except that the integral is terminated at the injection radius r_i not $r_{\max}$ since $dr/dz \neq 0$:

$$z_f = \frac{1}{\sqrt{2}} \int_{0.5}^{3.7} \frac{dr}{\sqrt{1.4 - \ln(r) - 1/2r^2}} = 3.8, \tag{10}$$

In unnormalized units, this corresponds to a new focal plane $f = \lambda z_f = 1.7$ cm., in excellent agreement with the results presented in Figure 6.

Returning to Figure 7, it is observed that for both distributions the asymptotic value of r_{rms} is nearly the same, however the beam with initial Gaussian distribution has a greatly increased emittance at the target, relative to the beam with uniform distribution. The increase in ϵ is due to a change in the distribution after the beam has passed through the new focal plane f. The initial and final radial distribution of the current density are plotted in Figure 8 for (a) the Gaussian and (b) the uniform distributions. It is observed that the uniform distribution remains nearly uniform at the target, whereas the Gaussian distribution at the target is distorted from Gaussian and has developed a wing at $r = 0.1$ cm. If in a real experiment the injected beam is more uniform than Gaussian only marginal emittance growth ($\sim 15\%$) is to be expected.

The emittance as a function of distance is plotted in Figure 9. The success of Eq. (10) in predicting the new focal plane is due in part on the assumption that ϵ remain constant during propagation. Indeed, for propagation prior to the focal plane f the beam compresses almost laminarly, and not until orbits have crossed near the focal plane does the emittance increase (although for the uniform distribution it is still only a marginal increase). This indicates that if the target is placed slightly upstream of the new focal plane, the emittance growth can be substantially limited.

The plasma plume will expand from the target at a rate such that for the duration of each pulse (e.g., 50 ns) the plasma will essentially be stationary. However, each subsequent pulse

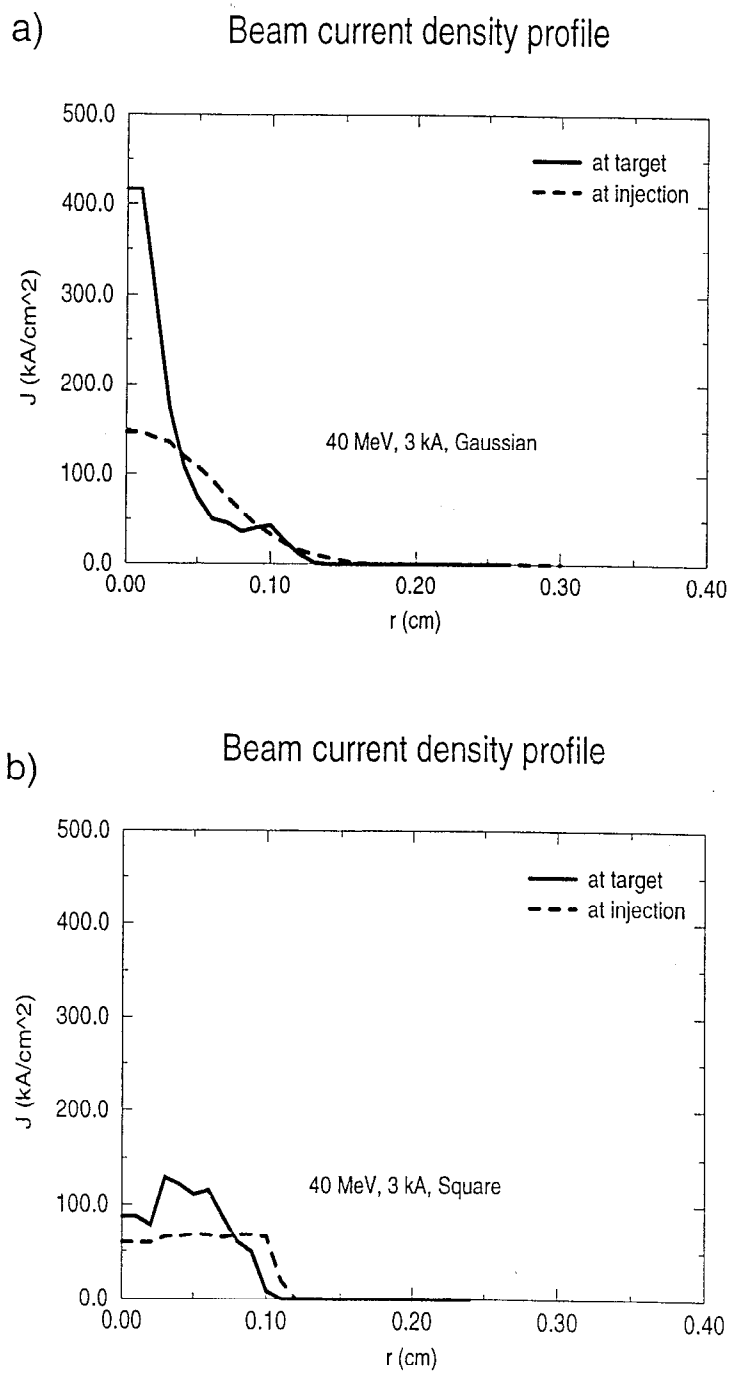

Figure 8: The beam current density at the injection plane and the target plane as a function of r for (a) the Gaussian beam, (b) the uniform beam.

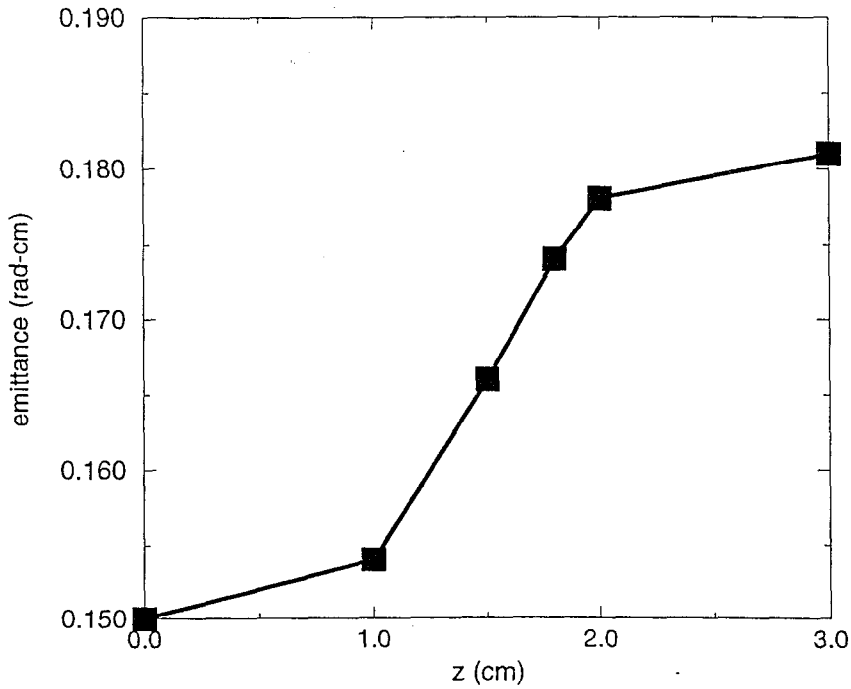

Figure 9: The beam emittance as a function of axial position.

will see a plasma of larger length. The simulations reported above considered a 3 cm plasma which is relevant for the 6th pulse in the train. Earlier pulses will pass through shorter plasma columns. In all cases, though, the beam will still focus before the target (provided the target is fixed at the focal plane position relevant for vacuum transport). However, since the "new" focal plane will be closer to the target for shorter plasma columns, we expect the spot-size on target to be smaller for shorter plasmas. On the other hand, since the emittance grows in the region around the focal plane and is essentially constant upstream and downstream of the focal plane, the emittance at the target should be invariant to the plasma length. In Figure 10, r_{rms} and ϵ are plotted as functions of time at the target for the beam with uniform distribution and varying plasma length.

2.4 Discussion

The presence of an over-dense, resistive, plasma in the propagation channel of an intense e-beam causes the beams' electrostatic electric field to be cancelled. In addition, because of the relatively short magnetic diffusion times $t_d \ll \tau$ for these very small submillimeter radius beams,

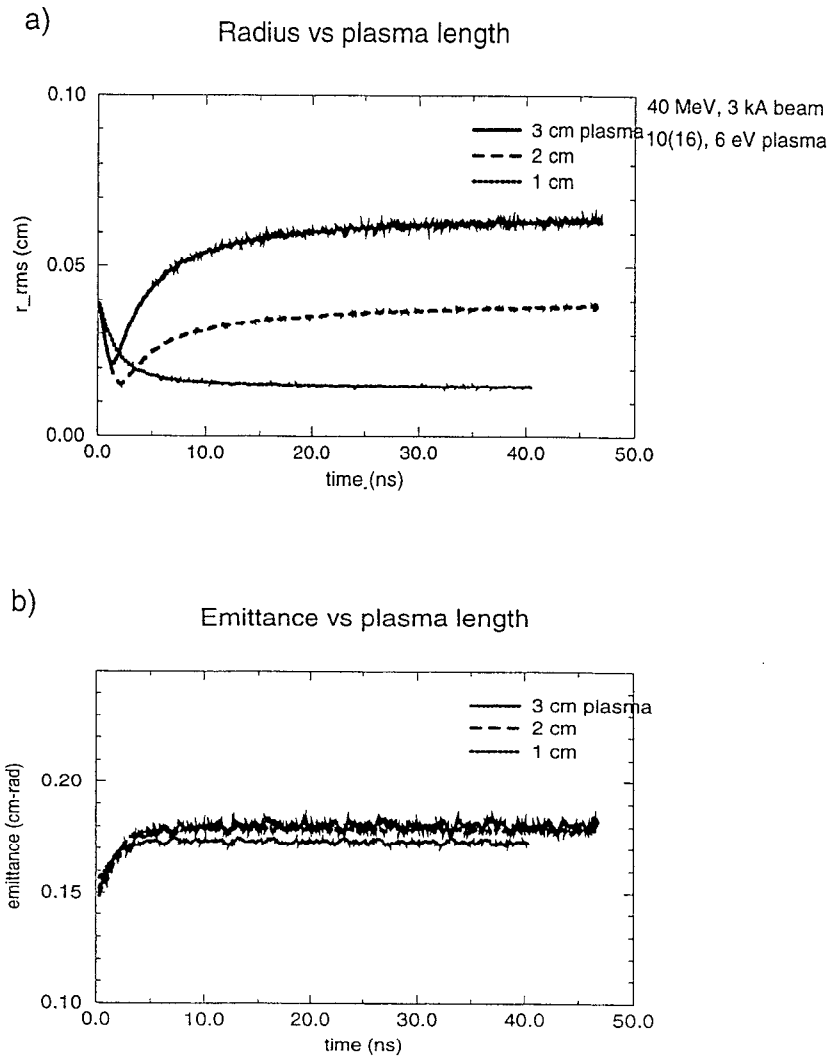

Figure 10: The beam (a) root-mean-squared radius (b) emittance at the target as functions of time for propagation in plasmas of different length. Results are presented for the beam with an initially uniform distribution.

the self-magnetic field is not shielded for times $t > t_d$. In this case the normal electrostatic repulsive force does not override the magnetic pinch force, and the beam pre-focuses. This increases the emittance on the downstream target and changes the beam profile and spot-size.

Fortunately, because the decay time is so short, the beam settles into a new equilibrium within a time $t \ll \tau$. In addition, under the influence of the pinch force, the beam compression is nearly laminar until reaching the first beam envelope minimum (the "new" focal plane). The emittance therefore remains nearly constant until the beam is within a few mm of the new focal plane. Hence, the axial position of the focal plane is predictable to a high degree of accuracy, and is a function of the incoming beam current, energy, radius, macro-angle, and emittance (all quantities which will be set and known upstream of the target-plasma interaction region). Because of this ability to predict the focal plane, it is therefore likely that corrective magnetic lenses can be employed to change the beams incoming focal properties such that the "new" focal plane remains at the target position. One can predict the necessary incoming beam conditions $(dr_i/dz, r_i)$ from Eqs. (8) and (9), given the focal distance $F = \pi/k$ and minimum required radius $r_{\min}$ (note that, as with the sample calculation Eq. (10), if $dr_i/dz \neq 0$ then $r_{\max} = r_i$). If, in addition, the corrective lenses are applied such that the target is always slightly upstream of the new focal plane, the emittance growth at the target should be minimal.

References

[1] Darwin Ho, private communication.

[2] B. V. Oliver and R. N. Sudan, Phys. Plasmas **3**, 4725 (1996).

[3] see, for example, J. D. Lawson, "The physics of charged particle beams," Oxford University Press, 1977.

3 Species Separation in Target Plasma

D. Welch

3.1 Introduction

Ions emitted from the focal spot of an electron beam can lead to charge neutralization of the beam and radius blowup [1]. Lighter ions such as protons have the ability to drift back and degrade the beam within 10 ns of emission. Singly charged heavy ions such as Ta^+ require a much longer time and will probably not impact a beam with a 50-ns pulse. In this section, we examine the physics of target plasmas. In particular, we look at ion selection and long time expansion of plasmas with multiple ion species.

The IPROP simulation code [2] can be used to model a pre-existing dense plasma or follow the desorption and breakdown of a neutral layer at the target. The new IPROP algorithm models collisions between charge particles and neutrals. Fields (either electrostatic or electromagnetic) and particle motion are solved implicitly. The collisions between charged particles occur at the Spitzer collision frequency. Interactions modeled for charged particle-neutral collisions include elastic and inelastic scattering (ionization and slowing down). Thus, IPROP is capable of simulating dense collisional plasmas and gases expected at the focal spot of an intense electron beam and long-time expansion between pulses.

In this section, we first present a quick summary of the IPROP algorithms used here to model target plasmas. We then describe the physics of multi-component ambipolar diffusion and present simulation results of beam-plasma interaction and inter-pulse plasma expansion.

3.2 Summary of IPROP algorithms

A 3-D implementation of the direct implicit particle-in-cell algorithm has been added to the IPROP code for static and electromagnetic field solvers [3]. The method is similar to that discussed by Hewett and Langdon for their 2-D AVANTI code [5]. The benefits of this treatment are that the usual limitations on time step, namely the need to resolve the cyclotron and plasma frequencies, are greatly relaxed. Also, the Debye length instability, responsible

for numerically heating a plasma until the Debye length is roughly the cell size, is nearly eliminated in useful regimes.

With the addition of the implicit capability, the higher densities and lower temperatures that we can simulate kinetically imply a larger collision rate. Therefore, we have developed an algorithm to model electron-electron, ion-ion and electron-ion collisions and collisions with neutrals. These models involve first constructing drifting Maxwellian distributions at each grid cell in each direction for plasma electrons, ions and neutrals. Each kinetic particle is first scattered isotropically in the center-of-mass frame off its own distribution. The probability of scatter is given by $P = \Delta t \min(\nu_m, c_s/\Delta x)$. Here, ν_m is the momentum exchange collision frequency, c_s is the sound speed of the particle species, and Δx is the grid cell length. If P were not limited by $c_s \Delta t/\Delta x$, we would experience a fluid Courant instability where information is transmitted faster than the speed of sound. To statistically conserve both momentum and energy, the probability of collision within and between species must be locally constant. This initial step preserves a Maxwellian distribution for a collisional plasma. It also pushes thermal conduction and includes pressure gradient forces and shock physics.

Collisions between different species are separated into an energy push and a frictional momentum push. The energy transfer from one species to another is accomplished by summing the temperature changes from each thermalization process. We assume the energy is transferred isotropically, but this step could be done for each direction separately. Finally, we rotate the particle velocity to account for elastic scatter. The particle velocity is first translated into the weighted scattering center-of-mass (COM) frame. After applying this rotation, the velocities are then placed back into the laboratory frame. The particle Lorentz force is modified to account for large momentum transfer frequency ν_m.

A known problem with the kinetic implementation is that if time steps are large, $t > 1/\omega_p$ (ω_p is the plasma frequency) and if electron particles cross more than half a cell in Δt, numerical cooling occurs. This is a noticeable problem in static field simulations where very large time steps are used with dense plasma problems. To circumvent this problem and achieve the desired speed up, we have included an implicit fluid model for the electrons.

The equation of motion for the fluid electrons is identical to that of a kinetic particle, except for scattering terms. A pressure gradient force term, to model electron-electron collisions, and a frictional force between the electron and other species replace elastic scattering events for

kinetic particles. The fluid modeling avoids much of the numerical cooling by including a separate equation for energy that includes PdV, energy exchange between species, flux-limited thermal conduction, ohmic heating and inelastic losses. Mean motion of the fluid particle can be converted into internal energy via collisions with neutrals and ions.

The internal energy for each particle is advanced and saved for the next time step. The energy conservation is quite good with this fluid algorithm at the large time steps desired for dense plasma modeling. However, in some circumstances, kinetic effects becomes important such as in runaway where a hot electron population coexists with a thermal one, and for less dense electrons accelerated from a cathode plasma. Thus, we need a hybrid, both kinetic and fluid, description for electrons.

In the hybrid mode, IPROP permits electron particles to be either fluid or kinetic. The criteria for changing from one component to the other is still being studied. At present, the criterion for a fluid electron to become a kinetic one is that the directed energy is much greater than the internal energy. A kinetic electron is converted into a fluid electron if its kinetic energy is less than the thermal energy of the ambient dense fluid. These criteria are best suited to having electrons, created in ionization, begin their life as fluid particles. Boundary emitted electrons begin as kinetic electrons.

IPROP also includes surface physics modeling. An initial quantity of contaminants (usually H_2) is loaded on a surface. Following particle heating and impact, these neutrals can then be liberated due to thermal and stimulated desorption. The neutrals can subsequently be ionized from charged particle collisions. This capability is used in Section 4.5.

These algorithms have been benchmarked against a known analytic two-dimensional ambipolar diffusion problem. We have also achieved good agreement with several experiments involving gas breakdown and dense plasma behavior.

3.3 Ambipolar diffusion

A high-β plasma expands due to the thermal pressure of all its constituents. If the plasma is much larger than a Debye length, it must remain nearly neutral. However, lighter particles, such as electrons, will attempt to move faster than the heavier particles. This motion causes a slight charge separation creating an electric field that attempts to drag the heavier particles

along. The potential associated with the separation is roughly $\phi = kT_e$. The effective diffusion coefficient $D = kT/m\nu_m$ of the ions is enhanced by the factor $1+T_e/T_i$. Thus, a non-equilibrium plasma with hot electrons will expand rapidly.

If two different weight ions exist in this expanding plasma, the lighter ions will accelerate more quickly under the influence of the field $E \approx kT_e/r$, where r is the radius of the plasma. If the collisionality (ν_m) of the plasma is weak, the lighter ions will expand faster than the heavier ones. The expansion time for an ion of mass m_i is given by,

$$t_{\text{exp}} = r\sqrt{2m_i/kT_e}. \tag{11}$$

Hotter electron temperatures and smaller plasma radii will enhance the expansion.

Ions of different mass can separate if,

$$\frac{v_{th}}{r\nu_m} > 1, \tag{12}$$

where v_{th} is the thermal velocity of the lighter ion. For singly charged ions, this inequality is satisfied for plasma with temperatures > 1 eV and densities $< 10^{16}$ cm^{-3}.

Now we consider a beam impacting a target plasma of 1-mm radius. Given a beam space charge potential $e\phi_b = 100$ keV and 5×10^{13} cm^{-3} impacting a plasma of density 5×10^{15} cm^{-3}. We can reasonably expect the electrons to heat to $T_e = e\phi_b n_b/n_p$ or roughly 1 keV. The proton expansion time for this case would be short, roughly 4 ns. This expansion time would permit a stratification of the lighter ions at larger radii and heavier ions at smaller radii near the beam. Simulations show this effect has important implications for beam neutralization.

3.4 Pre-existing plasma at target

We have speculated that a beam impinging on a heterogeneous target plasma would tend to select heavier ions over lighter ions, similar to the process discussed by Mendel [4] for ion diodes. If this were the case, the most dangerous ions for producing a "flying focus" would not be emitted from the plasma. Heavier ions such as C^+ or even metal ions would require 10's of nanoseconds to disrupt the beam. To study this hypothesis, we initialize a 3×10^{15} cm^{-3} maximum density plasma with 50% protons and 50% carbon ions. We simulated a uniform density plasma which extended 2-mm from the target and a plasma with density that falls

linearly to zero at 2-mm from the target surface. The results were similar for the two cases. A stiff (500 MeV) 2-kA (2-ns rise time), electron beam with 0.5-mm radius of uniform density is injected normally 3 cm from a tantalum target. The resolution at the plasma surface was 50 microns. The results were similar with cell sizes twice this size.

The simulations suggest that indeed the heavier ion dominates the neutralization process. The carbon ions exit the dense plasma at a smaller radius and thus neutralize the beam charge more efficiently even though the protons are emitted from the plasma with roughly the same density as C^+. The reason for this behavior is that the electrons heat and the plasma undergoes ambipolar diffusion radially as discussed above. The light electrons move outwards first, then the protons accelerate radially due to the excess positive charge. The heavier C^+ ions cannot react as fast as the protons and remain at a smaller radius.

The proton density as a fraction of the beam density away from the target is 0.2 with the C^+ fraction roughly 0.15. The radius of H^+ and C^+ is quite different as is shown at various times in Figures 11 and 12. We see the proton radius increases to 1.6 mm near the target by 20-ns and the emitted ions are 1–2 mm in radius (RMS). The C^+ radius increases to only 0.7 mm by 20-ns and the emitted C^+ remains roughly the beam radius. The effective neutralization of the beam charge is shown in Figure 13. The rate at which the neutralization moves out from the target more closely resembles the C^+ velocity than that of the protons. It took these ions 20 ns to reach the 3-cm position and only then did the neutralization fraction exceed 0.1 at that position. These results suggest that while some neutralization (5%) by the fast protons occurs, the nominal 25% neutralization moves back into the beam at the heavier ion velocity.

3.5 Plasma expansion between beam pulses

We now address the question of how much light-mass contamination of the target material is tolerable for the next pulse. We assume that the previous beam pulse has left an expanding plasma plume. A danger for the next pulse is that the light ions move towards the plasma surfaces and will provide a ready source for beam neutralization. In between pulses, the target plasma cools as it expands. The collisionality increases and the motion of the different ions becomes coupled at lower densities. This enhanced coupling inhibits the flow of light ions to the plasma edges.

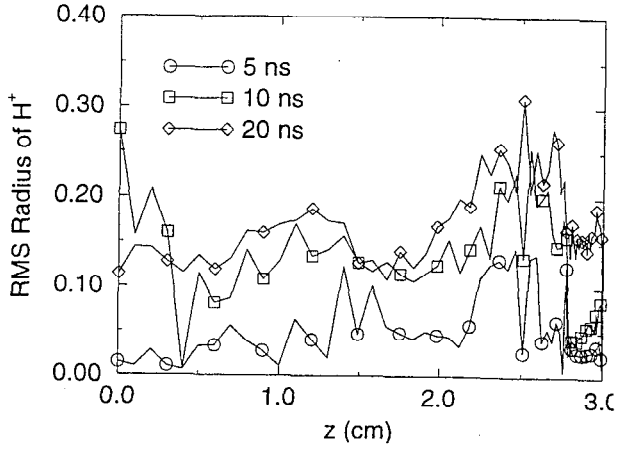

Figure 11: The proton radius is plotted for the ETA-II simulation after 5, 10 and 20 ns.

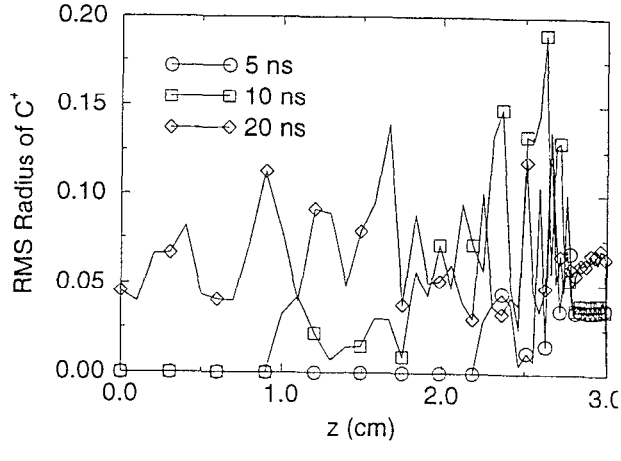

Figure 12: The carbon ion radius is plotted for the ETA-II simulation after 5, 10 and 20 ns.

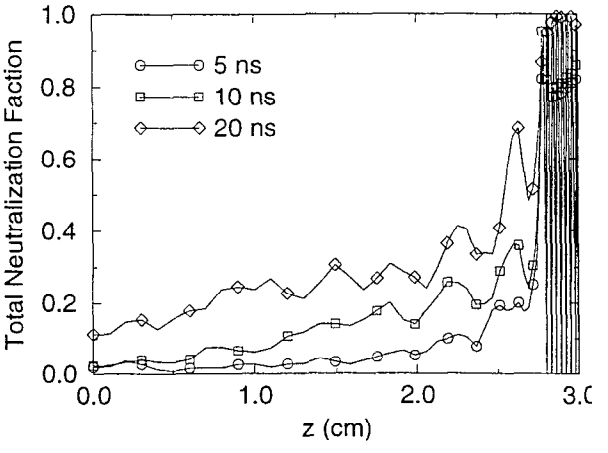

Figure 13: The total charge neutralization of the 2 kA beam is plotted for the ETA-II simulation after 5, 10 and 20 ns.

We now simulate a 2-D expanding multi-component plasma using IPROP with electrostatic fields which allows several microsecond time scales. The plasma was initialized in the center of a 1 cm $\times$ 1 cm conducting box. The plasma density was peaked on axis (10^{16} cm^{-3} density) with a $\cos(0.5\pi(x/1\text{ mm}))\cos(0.5\pi(y/1\text{ mm}))$ distribution. The temperature of all components was initially uniform at 1 or 4 eV. The plasma ions were 99% O^+ and 1% p^+.

The two simulations demonstrate the importance of the plasma temperature in determining whether the fraction of protons builds up on the plasma edge or not. In Figures 14 and 15, we see a cut of the densities of O^+ and p^+ through the $y = 0$ plane at different times. In the 4-eV case, the ions at the plasma edge are mostly protons after 133 ns, a factor of 100 increase in concentration. The density profile is fairly flat in x. By 266 ns, the O^+ and p^+ fractions are roughly equal at the edge with a 5×10^{11} density. Because the temperature was down a factor of four, we ran the 1-eV simulation out twice as far to see the same expansion. In this case, the momenta of the two ions are better coupled (roughly 10 times greater collision frequency) and the proton fraction does not increase significantly by 533 ns. The profiles are similar for the two ions.

From these simulations, we can expect lighter ions in the target plasma, fairly hot just after the initial beam pulse, to diffuse more rapidly. This is particularly true in the lower density front. After the plume has expanded, the ion concentrations will freeze progressively

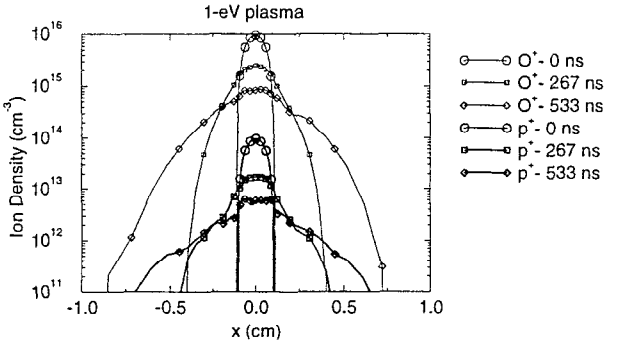

Figure 14: The p^+ and O^+ densities for the 1 eV IPROP simulation are plotted at 0, 266 and 533 ns.

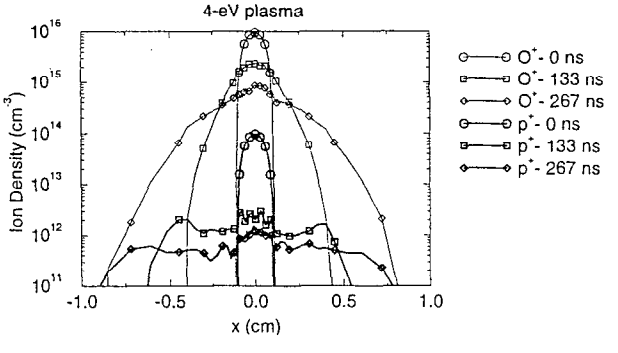

Figure 15: The p^+ and O^+ densities for the 4 eV IPROP simulation are plotted at 0, 133 and 267 ns.

at low densities. This process demands an upper bound on the initial fraction of light ions to be sufficiently small that a factor of roughly 100 increase (based on the 4-eV simulations) at the edges is tolerable. An estimate of the upper bound based on this logic is 10^{-5}–10^{-4} initial fraction of protons. A proton fraction this low in the bulk of the target material is recommended.

We should in the future consider what ion fraction a subsequent beam pulse would pull from a plume (both off and on axis) if the proton fraction is large on the edge. It is possible that the rapid diffusion of the protons would again occur which would quickly (in several nanoseconds) inhibit light ion neutralization and poor focusing. Such a result would relax the upper bound on the initial proton fraction.

References

[1] D. R. Welch and T. P. Hughes, Laser and Particle Beams **16**, 285-294 (1998).

[2] D. R. Welch, C. L. Olson and T. W. L. Sanford, Phys. Plasmas **1**, 764 (1994).

[3] D. R. Welch and B. V. Oliver, "Third Quarter 1998 Progress Report in Support of the ICF Program at Sandia National Laboratories," MRC/ABQ-R-1890 (1998).

[4] C. W. Mendel, Jr. and G. S. Mills, J. Appl. Phys., **53**, 7265-7273 (1982).

[5] D. W. Hewett and A. B. Langdon, J. Comp. Phys., **72**, 121- 155 (1987).

4 Effect of Adsorbed Surface Density On Ion Current Density

T. Hughes and D. Welch

4.1 Summary

In the ETA-II target experiments [1], a 2 kA. 5.5 MV electron beam is focused to a spot with a full-width-half-maximum of about 1 mm on a tantalum foil. The results do not show the type of "worst case" defocusing due to ion emission discussed in Ref. [2]. We have carried out some calculations which show that for an adsorbed areal density of $10^{15}\,\mathrm{cm}^{-2}$ (one monolayer), which is roughly the measured value on the ETA-II target, direct-impact ionization by the beam is insufficient to produce space-charge-limited ion flow. Furthermore, electron secondaries resulting from direct-impact ionization are driven rapidly into the target by the axial electric field of the beam, and as a result do not contribute significantly to the ionization fraction of the desorbed monolayer. The ionization due to ion-neutral collisions is also estimated to be small. Experiments where a laser is focused onto the target prior to the electron beam show strong disruption of the focus. The laser is thought to create a highly ionized plasma at the surface, in which case one monolayer can provide space-charge-limited ion flux, leading to rapid growth in the spot-size.

4.2 Estimate of beam-induced ionization

The mechanism for generating light ions at the target is thought to be as follows [3]. Beam electrons heat the surface to the point where physisorbed and chemisorbed species evaporate from the surface as gas-phase molecules. They are then ionized by the beam electrons and provide a source of light ions. The rate at which molecules desorb from a surface is modeled by

$$\frac{dN_d}{dt} = -\frac{dN_a}{dt} = N_a \nu_d e^{-Q/T}, \tag{13}$$

where N_d is the number desorbed per unit area, N_a is the number adsorbed per unit area, ν_d is a rate constant typically of order $10^{13}\,\mathrm{s}^{-1}$ [4], and Q is the binding energy of the adsorbed species. Binding energies typically vary from a fraction of an eV for physisorbed species to several eV for chemisorbed species, and depend on both the adsorbed species and the nature

of the substrate. At room temperature, the desorption e-folding time transitions from short (minutes) to long (hours) at $Q \approx 0.9\,\mathrm{eV}$.

The heating rate due to electron-beam impact is given by

$$\frac{dT}{dt} = \frac{1}{c_v}\frac{dE}{dx}\frac{I_b}{e\pi r_b^2}, \tag{14}$$

where c_v is the specific heat, dE/dx is the stopping power, I_b is the beam current, and r_b is the beam radius. For values typical of the ETA-II target experiments, for example, ($I_b = 2\,\mathrm{kA}$, $r_b = 0.6\,\mathrm{mm}$, Ta target) this gives a heating rate of $0.12\,\mathrm{eV/ns}$. From Eq. (13), the desorption e-folding time is $\leq 1\,\mathrm{ns}$ for $T \geq Q/9$. Thus, even for species with binding energies of several eV, there is substantial desorption after just a few ns.

Once the species have desorbed, they can undergo gas-phase ionization by the beam electrons. The electron impact-ionization cross-section as a function of energy is shown in Figure 16. At the beam energy of 5.5 MV, the cross-section is $\sigma_b \approx 2 \times 10^{-19}\,\mathrm{cm}^2$.

It is well-known that for gas pressures above a Torr or so, an ionization avalanche can be produced by secondary electrons because they are accelerated by the beam's electric field to energies near the peak of the cross-section in Figure 16. To see if this effect might contribute to the ionization of desorbed molecules, we estimate the mean-free path, λ, of a secondary electron, in units of the thickness of the desorbed layer Δx as

$$\frac{\lambda}{\Delta x} = \frac{1}{N_d \sigma_{\max}}, \tag{15}$$

where N_d is the desorbed areal density and $\sigma_{\max}$ is the peak ionization cross-section. For one desorbed monolayer ($N_d \approx 10^{15}\,\mathrm{cm}^{-2}$) and $\sigma_{\max} \approx 10^{-16}\,\mathrm{cm}^2$, $\lambda \approx 10\Delta x$, so that the secondaries produce little extra ionization, unless they are somehow confined in the vicinity of the desorbed neutrals.

Near the target, the dominant self-fields of the beam are the axial electric field and the azimuthal magnetic field. The trajectory of a secondary born in these crossed fields is cycloidal (see Fig. 17), with the amplitude of the cycloid given by (MKS units)

$$r_c = \frac{2m_e E_z}{eB_\theta^2} \approx \frac{r_b}{\nu}, \tag{16}$$

where r_b is the beam radius and ν is Budker's parameter (≈ 0.1 for the ETA-II beam). Thus, on the axial length-scale of the desorbed monolayer, the trajectory is almost a straight line into

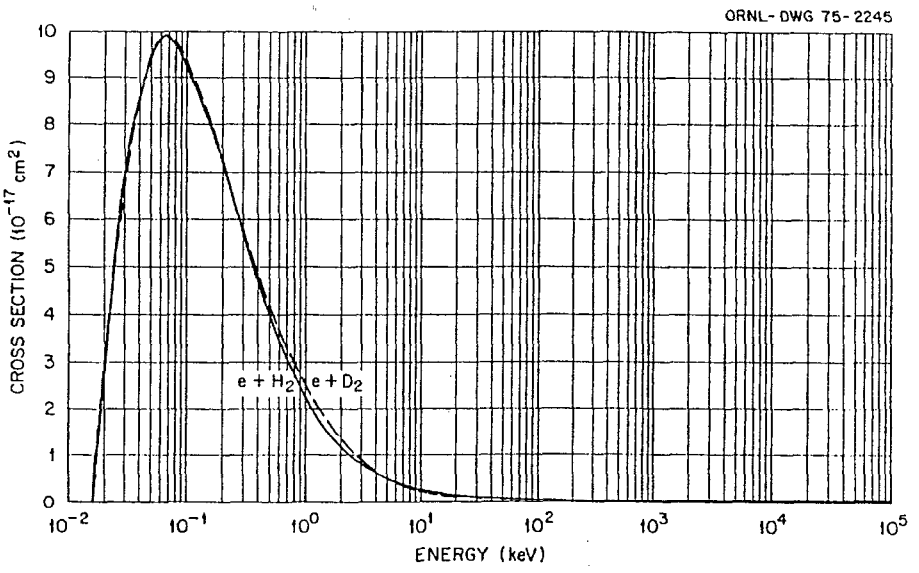

Figure 16: Electron impact ionization cross-section for $H_2 + e \rightarrow H_2^+ + 2e$ as a function of energy (from Ref. [5]).

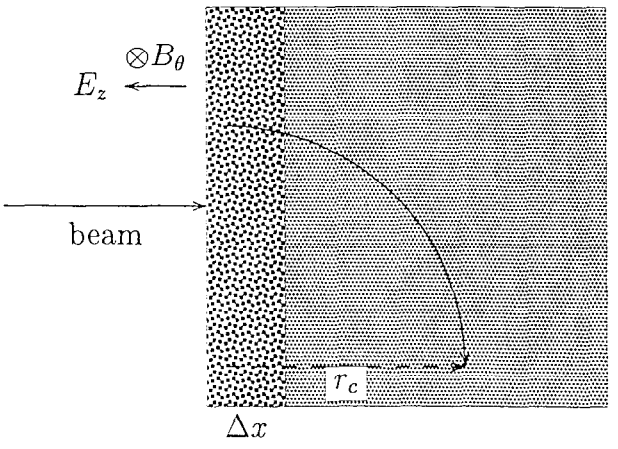

Figure 17: Orbit of a secondary electron near the target. The thickness of the desorbed layer is Δx.

the target, i.e., the secondaries escape and contribute little additional ionization. If there are sufficiently many monolayers (10 or more) so that the space-charge-limited ion emission reduces the electric field at the surface to zero, then the secondaries may be trapped in the self-magnetic field of the beam and create an avalanche. Thus, it appears that avalanche ionization of the desorbed neutrals can occur only when space-charge-limited ion emission is already taking place due to primary beam ionization.

From Ref. [2], the space-charge-limited ion current drawn by the beam at the target is given by

$$\frac{I_i^{scl}}{I_b} \approx 0.56 \left(\frac{Z^* \nu}{A} \right)^{\frac{1}{2}}, \tag{17}$$

where Z^* is the charge-state and A is the atomic or molecular number of the desorbed species. The ion current due to direct-impact ionization is given by

$$\frac{I_i^{dii}}{I_b} \approx \sigma_b N_d. \tag{18}$$

In the absence of some additional ionization mechanism, the actual current drawn by the beam will be the smaller of I_i^{scl} and I_i^{dii}. Assuming that one monolayer has an areal density of $10^{15}\,\mathrm{cm}^{-2}$, and that $\sigma_b \approx Z \times 10^{-19}\,\mathrm{cm}^2$, where Z is the atomic or molecular number of the desorbed species, we can estimate the number of monolayers required to produce the space-charge-limited ion current:

$$N_{ml} \approx 5600 \left(\frac{Z^* \nu}{A Z^2} \right)^{1/2}. \tag{19}$$

This is plotted in Figure 18, where we see that for the ETA-II beam current, over 10 monolayers of H_2 are required.

The variation with pressure of the number of monolayers on a surface in equilibrium with a gas is given by the adsorption isotherm $f_T(p)$. Five types of adsorption isotherms, shown in Figure 19, have been observed experimentally [6]. Several theories, all involving surface- and adsorbate-specific parameters, have been developed to explain these shapes. At sufficiently low pressures and surface coverage, all isotherms tend towards Henry's Law, which states that the surface coverage is proportional to pressure. The pressure below which this behavior applies can only be determined experimentally. Some low-temperature (77 K) measurements [7] indicate that it applies only at extremely low pressures ($< 10^{-10}$ Torr), and that the pressure dependence is much weaker at higher pressures. The Temkin isotherm, which agrees with pump-down data

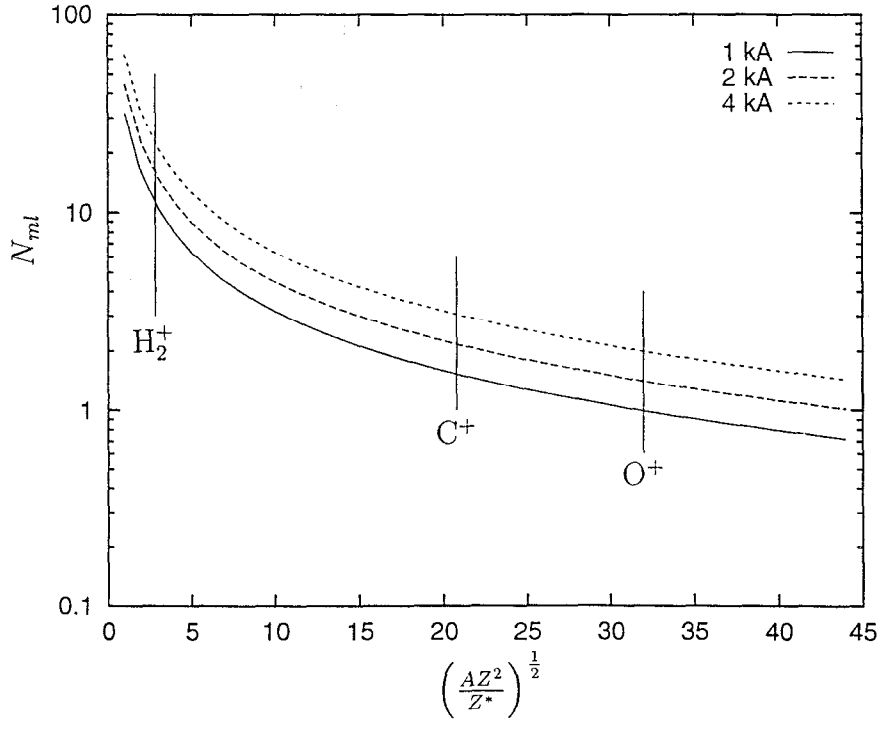

Figure 18: Number of monolayers required to yield space-charge-limited ion current.

for adsorbed water-vapor [8], has a weaker, logarithmic dependence on pressure above pressures of about 10^{-7} Torr.

Even if the adsorption isotherm were known for a given experimental configuration, this information is of little use in computing the actual surface coverage at room temperature for binding energies Q larger than about 1 eV. For example, for $Q = 1.2$ eV, the timescale on which the surface coverage reaches equilibrium is over a year according to Eq. (13). In practice, the surface coverage needs to be measured directly, and near the time at which beam data are taken.

4.3 Estimate of ion-induced ionization

Another source of ionization is due to ion-neutral collisions. The cross-section for ionization of H_2 by H^+ peaks at about 1.7×10^{-16} cm^{-2} near 50 keV, as shown in Fig. 20. Ions can reach this energy in a distance of order 100 μm from the surface, and the desorbed neutrals drift several times this distance during a 50 ns pulse. However, for areal densities of order 10^{15} cm^{-2}, an

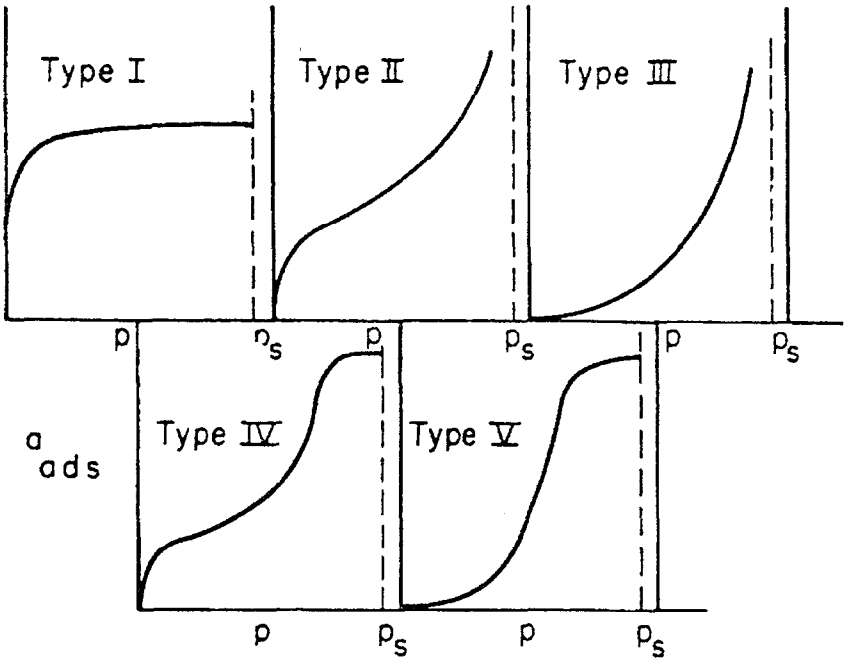

Figure 19: The five types of vapor adsorption isotherms, where p_s is the "saturation pressure" (Ref. [6]). Types IV and V are for porous substrates.

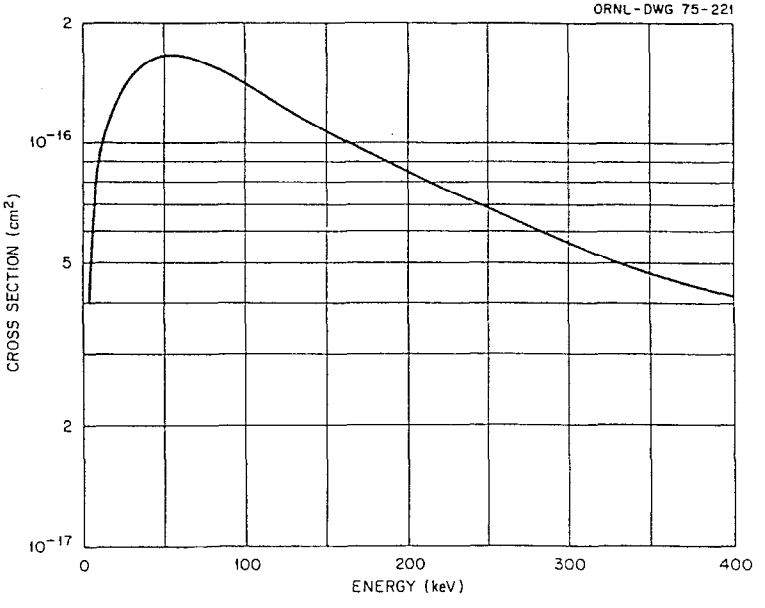

Figure 20: Cross-section for the ionization process $H^+ + H_2 \rightarrow H^+ + H_2^+ + e$ (from Ref. [9]).

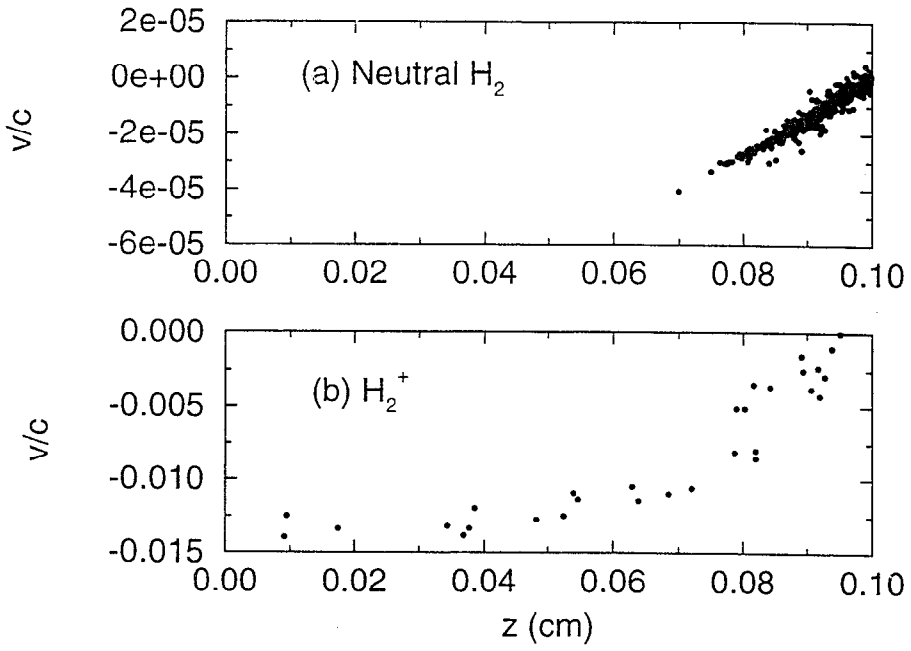

Figure 21: Longitudinal phase-space of (a) desorbed neutrals and (b) ions after 30 ns.

ion on average can produce only about 0.2 additional ions as it transits the neutral layer. Ion-neutral collisions may contribute significantly to ionization when many monolayers are present.

4.4 1-D simulations of desorption

To model the desorption and ionization processes discussed in the previous section, we conduct 1-D IVORY simulations (the grid is in the direction of beam propagation). A monolayer of atomic hydrogen ($\approx 10^{15}\,\mathrm{cm}^{-2}$) is adsorbed onto the surface with a binding energy of 1.1 eV. The binding energy for H_2 on metals lies in the range of 10–40 kcal/mol, or 0.4–1.7 eV [10]. A 5.5 MeV beam with a current density of $125\,\mathrm{kA/cm}^2$ (1.4 kA on a 0.06 cm radius spot) is incident on the target, and we simulate a 1 mm region out from the target using 10 μm cells. We model the following processes: heating of the target surface due to electron impact, thermal desorption of neutrals, and beam-neutral, secondary electron-neutral and ion-neutral ionization. We find that the entire monolayer desorbs from the surface in about 3 ns. A plot of the phase-space of the neutrals and ions after 30 ns is shown in Figure 21.

At that time the peak neutral H_2 velocity is $v/c \approx 3 \times 10^{-5}$, or about 1 cm/$\mu$sec, and the peak H_2^+ velocity is about 400 cm/μs.

Direct-impact ionization by the beam leads to an ion current-density equal to about 2×10^{-4} of the beam current density. For H_2^+ ions, this implies an upstream charge-density fraction $f = 0.011$, assuming a 300 kV on-axis beam potential. For space-charge-limited emission, the fraction is $f = 0.15$, about 13 times larger.

4.5 Multi-Monolayer simulations

In a second set of simulations using IPROP, we initialized the target surface with 2.5, 5 or 10 monolayers of H_2. After the target heats to a few hundred degrees the neutral gas is released from the surface with the surface temperature. The surface heats initially at the same rate in each of the simulations reaching 8 eV in 20 ns. Some enhanced heating occurs in the higher monolayer simulations due to the deposition of plasma electron energy. The 2.5 and 5 monolayer runs reached a steady state by 15 ns where only beam-ionized hydrogen ions provided neutralization. The simulations did not show a neutral layer breakdown (simulations were run to 25 ns), except in the 10 monolayer case. Thus, the neutralization was well below the space-charge-limited 25% value in those simulations as is shown in Figure 22. Back from the target surface, the 2.5 and 5 monolayer simulations had 6% and 12% neutralization, respectively. (The fractional neutralization is higher than that in Section 4.4 because the upstream potential here is lower, so the ions move more slowly.) These simulations show that $\sim$ 10 monolayers of hydrogen are required for the layer to break down into a dense plasma that would provide full Child-Langmuir emission.

4.6 2-D simulations of beam spot

To see the effect of source-limited emission on the beam spot, we carried out 2-D simulations using the LSP code. We assumed beam parameters of 2 kA, 5.5 MV and normalized edge emittance of 1000 mm-mrad. The target is located 8 cm past the center of the final-focus magnet and the beam is injected 22 cm upstream of the center of the magnet. We ran a source-limited case assuming an ion-creation rate given by Eq. (18), i.e., each beam electron has a probability of 2×10^{-4} of creating an ion. A particle plot after 40 ns is shown in Figure 23.

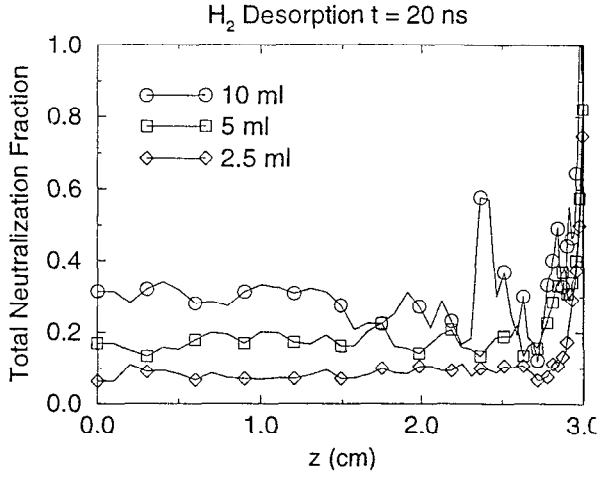

Figure 22: The total charge neutralization of the 2 kA beam in the three desorption simulations is plotted 20 ns into the IPROP simulations.

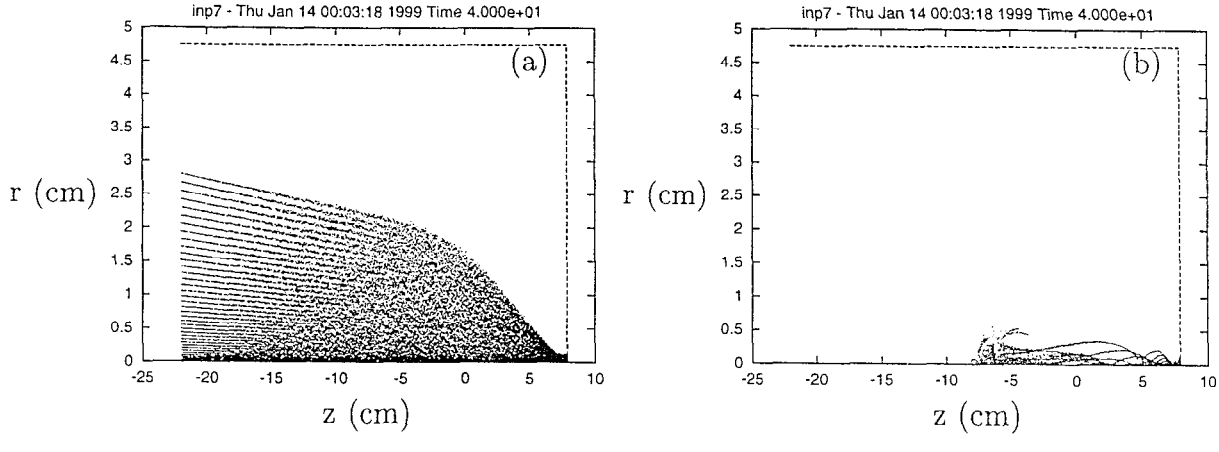

Figure 23: Plot of (a) beam electrons and (b) emitted H_2^+ ions after 40 ns. Final-focus magnet is centered at $z = 0$.

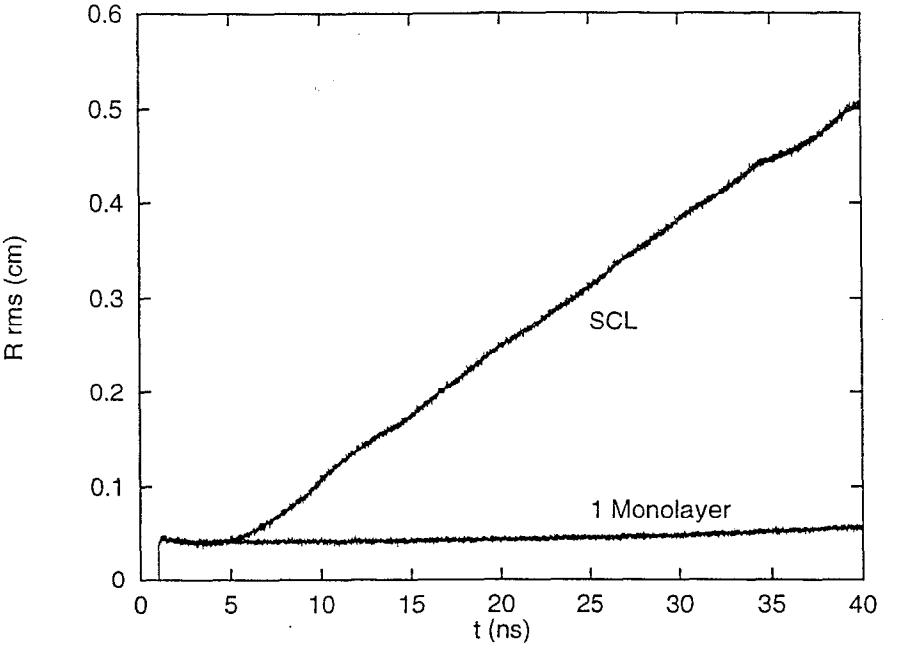

Figure 24: Comparison of beam-spot radius growth for space-charge-limited ion emission (SCL) and source-limited ion emission. Ion species is H_2^+.

Comparing this to the space-charge-limited case in Figure 24 we see that the disrupting effect of the backstreaming ions is much reduced when only 1 monolayer is available. The *rms* radius grows from 0.045 cm to 0.057 cm for the source-limited case, and to 0.5 cm for the space-charge-limited case.

A similar comparison for C^+ ions is shown in Figure 25. The difference is less dramatic, as expected from Figure 18, since fewer monolayers of C^+ are required to provide the space-charge-limited current. The spot-size growth with 1 monolayer of C^+ is actually larger than for 1 monolayer of H_2^+: the *rms* radius grows from 0.045 cm to 0.083 cm. This agrees with a scaling argument based on the "disruption time" [2], which is the time it takes the backstreaming ions to overfocus the beam:

$$t_d \approx \frac{r_s}{\beta_i c}\left(\frac{2\gamma}{f\nu}\right)^{\frac{1}{2}} \tag{20}$$

where r_s is the spot-size, β_i is the normalized ion velocity and f is the neutralization fraction due to the ions. For space-charge-limited emission, f is a constant [2], so $t_d \propto 1/\beta_i \propto \sqrt{A/Z^*}$. Thus, heavier ions take longer to disrupt the focus. For source-limited emission, however, the neutralization fraction is

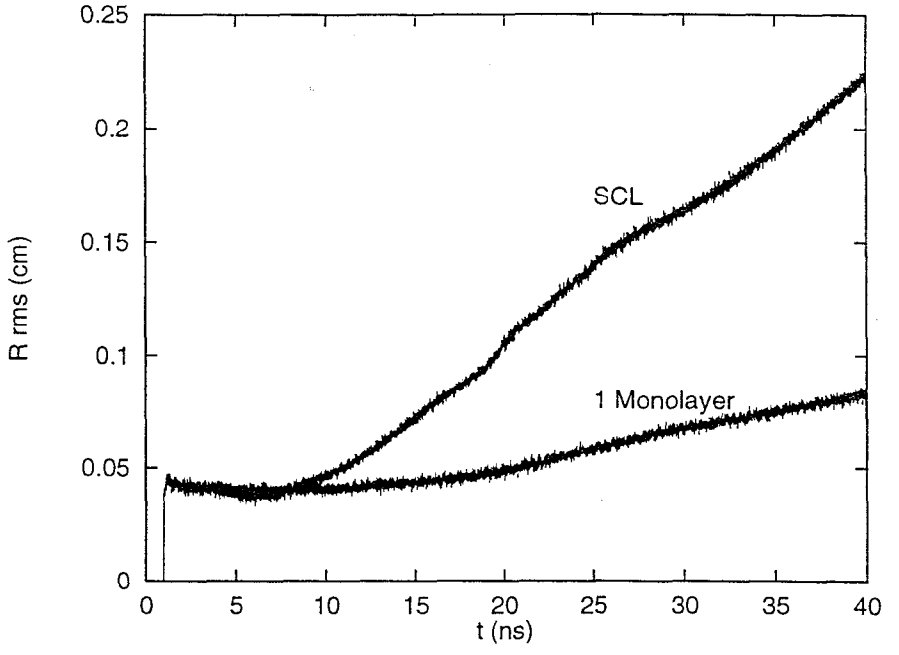

Figure 25: Comparison of beam-spot radius growth for space-charge-limited ion emission (SCL) and source-limited ion emission. Ion species is C^+.

$$f = \frac{\sigma_b N_{ml}}{\beta_i} \tag{21}$$

so that $t_d \propto (A/Z^2 Z^*)^{1/4}$. Since $A \approx 2Z$, the disruption time decreases for heavier ions. Essentially, the scaling becomes dominated by the fact that it is easier to ionize atoms which have more electrons.

These results may explain why minimal spot-size disruption was observed in ETA-II experiments [1]. In experiments where a low-energy laser was focused onto the target prior to the electron beam, strong disruption of the spot was observed. A crude calculation assuming deposition of 50 mJ in a depth of one wavelength (1.06 μm) at the critical density ($10^{21}\,\mathrm{cm}^{-3}$), in a spot of radius 0.05 cm, gives a temperature rise for tantalum of about 100 eV. We therefore speculate that the laser produces a highly-ionized plasma at the target surface. Just one fully-ionized monolayer can easily supply the space-charge-limited current. From Eq. (17), the H_2^+ current is about 6 A for a 2 kA electron beam, which requires 2×10^{12} ions over a 50 ns pulse. A spot of 0.05 cm radius covered in 1 monolayer contains about 8×10^{12} atoms.

In the laser experiments, an ion signal is detected on Faraday cups 25 cm from the target about 20 ns after the end of the beam pulse. This is qualitatively consistent with calculations carried out for the 4 kA ITS experiment [11], using C^+ as the ion species. The ions, which are electrostatically confined during the beam pulse, began arriving at the wall about 30 ns after the end of the beam pulse.

References

[1] S. Sampayan, G. Caporaso, Y.-J. Chen, C. Crist, M. Garcia, T. Houck, M. Krogh, R. Richardson, J. Weir, and G. Westenskow. Experimental investigation of beam optics issues at the bremsstrahlung converters for radiographic applications. In *Proceedings of 1998 Linac Conference*, 1998.

[2] D. R. Welch and T. P. Hughes. Effect of target-emitted ions on the focal spot of an intense electron beam. *Laser and Particle Beams*, 16(2):285–294, 1998.

[3] T. W. L. Sanford, J. A. Halbleib, J. W. Poukey, A. L. Pregenzer, R. C. Pate, C. E. Heath, R. Mock, G. A. Mastin, and D. C. Ghiglia. Measurement of electron energy deposition necessary to form an anode plasma in Ta, Ti, and C for coaxial bremsstrahlung diodes. *J. Appl. Phys.*, 66:10, 1989.

[4] D. Lichtman. Surface physics. In G. L. Weissler and R. W. Carlson, editors, *Vacuum Physics and Technology*, number 14 in Methods of Experimental Physics. Academic Press, New York, 1979.

[5] C. F. Barnett, J. A. Ray, E. Ricci, M. I. Wilker, E. W. McDaniel, E. W. Thomas, and H. B. Gilbody. Atomic data for controlled fusion research. Technical Report ORNL-5207, Oak Ridge National Laboratory, February 1977. (Vol. II of ORNL-5206).

[6] S. Brunauer and L. E. Copeland. Surface tension, adsorption. In E. U. Condon and H. Odishaw, editors, *Handbook of Physics*, chapter 7. McGraw-Hill, New York, second edition, 1967.

[7] J. P. Hobson. Analysis of ultrahigh vacuum isotherm data with the Brunauer-Emmett-Teller equation. *J. Vac. Sci. Technol. A*, 14(3):1277, 1996.

[8] P. A. Redhead. Modeling the pump-down of a reversibly adsorbed phase. I. Monolayer and submonolayer initial coverage. *J. Vac. Sci. Technol. A*, 13(2):467, 1995.

[9] C. F. Barnett, J. A. Ray, E. Ricci, M. I. Wilker, E. W. McDaniel, E. W. Thomas, and H. B. Gilbody. Atomic data for controlled fusion research. Technical Report ORNL-5206, Oak Ridge National Laboratory, February 1977. (Vol. I).

[10] M. E. Cuneo, P. R. Menge, D. L. Hanson, W. E. Fowler, M. A. Bernard, G. R. Ziska, A. B. Filuk, T. D. Pointon, R. A. Vesey, D. R. Welch, J. E. Bailey, M. P. Desjarlais, T. R. Lockner, T. A. Melhorn, S. A. Slutz, and M. A. Stark. Results of vacuum cleaning techniques on the performance of LiF field-threshold ion sources on extraction applied-B ion diodes at 1-10 TW. *IEEE Trans. Plasma Sci.*, 25(2):229, April 1997.

[11] T. P. Hughes. Target calculations for ITS short-focus experiment. Technical Report MRC/ABQ-N-589, Mission Research Corporation, September 1997.